Dynamic behavior of soft, resonant metamaterials: Experiments and simulations

(iD) **Bryan Chem,** (iD) **Yijie Jiang,** (iD) **Chenchen Liu, et al.**

COLLECTIONS

Paper published as part of the special topic on Acoustic Metamaterials 2021

View Online   Export Citation   CrossMark

ARTICLES YOU MAY BE INTERESTED IN

Nonlinear waves in flexible mechanical metamaterials
Journal of Applied Physics **130**, 040901 (2021); https://doi.org/10.1063/5.0050271

Propagation and attenuation of Rayleigh and pseudo surface waves in viscoelastic metamaterials
Journal of Applied Physics **129**, 124903 (2021); https://doi.org/10.1063/5.0042577

Acoustic metamaterials
Journal of Applied Physics **129**, 171103 (2021); https://doi.org/10.1063/5.0046878

Dynamic behavior of soft, resonant metamaterials: Experiments and simulations

Bryan Chem, [iD] Yijie Jiang, [iD] Chenchen Liu, [iD] Jordan R. Raney, [iD] and Celia Reina[a] [iD]

AFFILIATIONS

Department of Mechanical Engineering and Applied Mechanics, University of Pennsylvania, Philadelphia,
Pennsylvania 19104, USA

Note: This paper is part of the Special Topic on Acoustic Metamaterials 2021.
[a]**Author to whom correspondence should be addressed:** creina@seas.upenn.edu

ABSTRACT

Though additive manufacturing and novel optimization techniques have led to many recent advances in elastic metamaterials, difficult fundamental challenges (e.g., narrow bandgaps) and practical challenges (e.g., dissipation and friction) remain. This work introduces simple and hierarchical resonant metamaterials made of soft polydimethylsiloxane rubber and removable steel insets. The additively manufactured samples are able to produce bandgaps with a gap–midgap ratio of 81.8%, which surpasses the majority of resonant, metamaterials of the same class and greatly outperforms analogous resonant structures with a stiff epoxy matrix. The role of several physical features on the transmission loss (TL) curve is assessed in detail numerically and compared to the experimental TL data. Matrix compliance is found to be a rich mechanism for bandgap widening with a dual effect: it deepens the traditional resonant bandgaps, and it can selectively shift certain vibrational modes to lower frequencies and aid in the merging of multiple bandgaps. This can lead to an overall increase of the bandgap width of over an order of magnitude. Viscous dissipation, friction, and the stochastic nature of geometrical inaccuracies common in additive manufacturing were also found to shape the TL curve and associated bandgaps to various degrees. Some of these mechanisms, combined with a soft frame, can further help merge bandgaps in rainbow or hierarchical designs and form ultrabroad, subwavelength bandgaps.

Published under license by AIP Publishing. https://doi.org/10.1063/5.0042456

I. INTRODUCTION

Elastic metamaterials possess properties that are not found in natural materials such as negative effective density and elastic moduli.[1,2] These properties have proven useful for the mitigation of propagating waves,[3] waveguiding,[4] subwavelength imaging,[5] cloaking,[6] and other novel applications.[7] With specially engineered microstructures, elastic metamaterials can utilize local resonances to generate frequency bandgaps where no waves may propagate.[3] These bandgaps, termed "subwavelength," occupy a range of frequencies lower than bandgaps produced by the Bragg scattering mechanisms used in phononic crystals; however, they typically cannot achieve wide frequency ranges.[2] Narrow bandwidths limit the range of achievable operating frequencies and, therefore, the practicality of such materials.

Bandgap broadening has been the subject of many studies, both by a careful choice of the constituent materials and their arrangements. On the materials side, the inclusion of viscoelastic materials can broaden bandgaps and shift the location of bandgaps.[8–10] The former effect can aid in merging neighboring bandgaps to produce a single, wider region of wave attenuation. In terms of microstructural arrangement, many studies have proposed graded or "rainbow" designs[11–14] that combine internal resonators possessing different resonant frequencies to produce a bandgap wider than any one of the single resonators alone. Random arrangements of resonators with different resonant frequencies produce a similar effect and, in some cases, wider bandgaps are achieved as compared to more structured configurations.[14] Hierarchical elastic metamaterials containing multiresonant structures have also been explored, and their graded configuration has been shown to exhibit ultrabroadband filtering capabilities.[15,16] More broadly, mechanical instabilities[17,18] and piezoelectric materials[19] can provide mechanisms for bandgap tunability.

Here, we investigate additively manufactured samples using Direct-Ink-Writing (DIW) to construct resonant structures with

soft polydimethylsiloxane (PDMS) rubber, which are complemented with modular steel insets to produce the local resonance effect required for the formation of subwavelength bandgaps. These resonant structures are further embedded in a PDMS matrix leading to highly modular resonant metastructures that enable both singly and multiply resonant behavior. Experimentally measured transmission loss (TL) curves for these samples indicate that their normalized bandwidth (the so-called gap–midgap ratio, later defined in detail) greatly exceeds that of most resonant metamaterials as well the performance of similar samples fabricated with epoxy matrices. Subsequent analyses show that most of this increase in bandwidth can be directly attributed to the difference in compliance in the matrix phase. We explain the multi-faceted mechanism behind this bandgap widening in later in the paper.

Consideration of elastic properties alone is, however, insufficient to achieve a quantitative comparison between computational and experimental results. Indeed, the complexities of the materials' constituent behavior, final geometry, and experimental setup of 3D printed samples often greatly exceed the simplifying assumptions made in conceptual designs. In an effort to improve modeling fidelity and inform the construction of additional additively manufactured elastic metamaterials, we examine the effect of the viscoelastic properties of the material, friction, and stochasticity in the geometry on the transmission loss curves and evaluate their contribution toward an increased agreement with experimental data.

We begin in Sec. II by describing the design of the single and multiresonator structures considered, the testing methods and their associated transmission loss curves. Next, in Sec. III, the modeling and simulation techniques are provided, and a detailed discussion on the effect of the various physical mechanisms on the TL curves is presented in Sec. IV. Final conclusions are then provided in Sec. V.

II. DESIGN AND TESTING

The elastic metamaterials include a "frame" with a rectangular grid of square unit pockets and steel insets connected to the former with slender PDMS beams. The resulting structures are depicted in Figs. 1(a) and 1(b) for the case of a PDMS frame and Fig. 14 for an epoxy frame. We remark that more unit cells usually means better wave attenuation performance but achieving this effect using the least number of unit cells possible (i.e., with a compact structure) is attractive for real world applications.

The steel insets considered (here labeled as L1 insets) have a thin-wall square cross section and protrude out of the plane of the frame as depicted in Figs. 1(b) and 1(c). This protrusion enables larger resonator masses and, consequently, lower bandgap frequencies. In addition, smaller steel cubes wrapped in a PDMS frame (L2 insets) can be nested inside of the L1 insets to produce a hierarchical resonant structure with an additional resonant frequency and associated bandgap. The reconfigurability enabled by the removable L1 and L2 insets is here exploited to analyze three different configurations and their associated dynamic properties (e.g., bandgaps' widths and depths)

- Configuration 1: All unit cells have L1 insets.
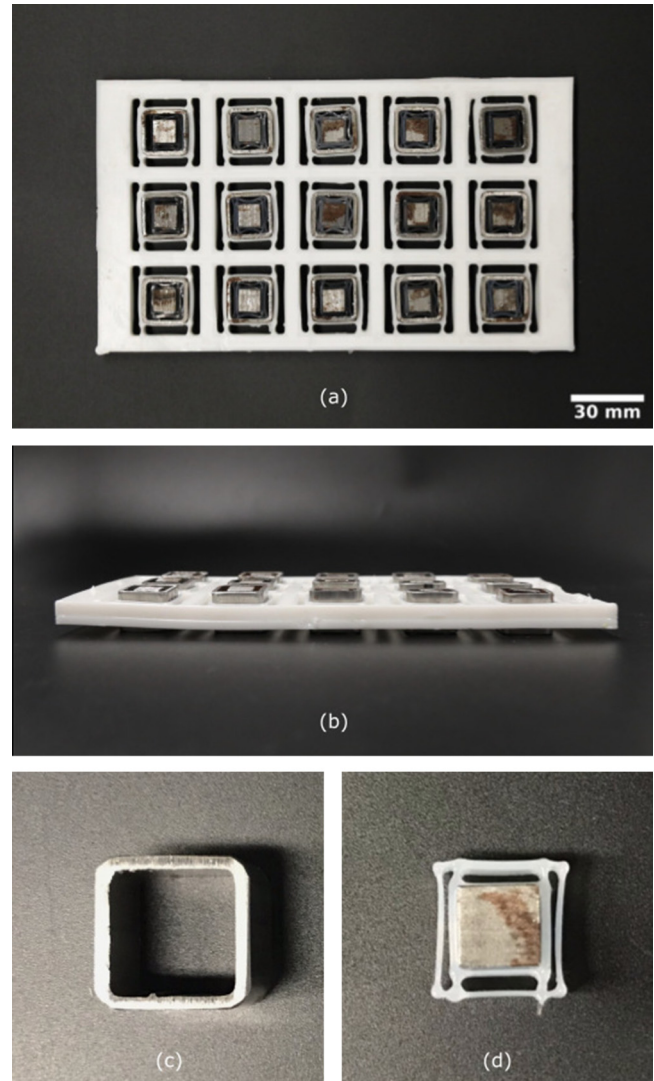
FIG. 1. (a) Elastic metamaterial with PDMS frame and both L1 and L2 insets. (b) Side profile of the elastic metamaterial (c) L1 inset. (d) L2 inset.

- Configuration 2: All unit cells have L1 and L2 insets.
- Configuration 3: All unit cells have L1 insets but only the first, third, and fifth columns of unit cells have the L2 insets.

The dynamic behavior of these metamaterials is examined in a horizontal configuration, with the steel insets that protrude from the frame resting on a glass surface. Lubricant oil is applied between the glass and the steel in order to reduce the effects of friction. A mechanical shaker is attached to one end of the sample, and piezoelectric accelerometers are attached to the two ends, collecting the input and output signals. A sinusoidal wave with frequency sweep from 30 to 250 Hz is set at the input end, and after a collection time of 1 s, the absolute value of the displacement at each sampling point is integrated and used to calculate the overall

transmission loss (TL) in the sample as

$$\text{TL} = 10 \log \frac{u_{out}}{u_{in}}. \qquad (1)$$

Here, u_{in} and u_{out} are the time integrals of the absolute value of the displacement at the input and output of the sample, respectively. Further details about the material fabrication and experimental processes are given in Appendix A.

The resulting transmission loss curves for the samples with epoxy and PDMS frames, both with simple resonant units (i.e., not hierarchical) are represented in Fig. 2 with the bandgaps from the epoxy frame and PDMS frame highlighted in gray and red, respectively. As it may be there observed, there is a dramatic difference between the two sets of samples: the structures with epoxy lead to a narrow and very shallow bandgap, while the designs with PDMS frame showed significantly wide bandgaps for a resonant structure. It is worth noting that in both cases, the resonant units are based on steel insets and PDMS beams. As a quantitative measure to compare the bandwidth across bandgaps of different depth and frequencies of operation, we use the gap–midgap ratio (GMGR)[20]

$$\text{GMGR} = 100 \left[\frac{2(f_{\text{high}} - f_{\text{low}})}{f_{\text{high}} + f_{\text{low}}} \right] \%, \qquad (2)$$

which represents a normalized bandwidth. Here, the edges of the bandwidth, f_{low} and f_{high}, are defined as the frequency values where the TL achieves half the minimum value of the corresponding bandgap. Using this metric, we find that the epoxy framed sample has a GMGR of 3.2%, while the PDMS framed sample has a much larger GMGR of 57.6%.

The marked difference between the two types of frames (Fig. 2) indicates that the material in which the resonant units are embedded strongly influences the observed behavior. At first glance, the most obvious difference between epoxy and PDMS is the strong contrast in their elastic constants (about three orders of magnitude). Further physical mechanisms that could contribute to widening of the bandgaps are material viscoelastic properties and friction between the metal insets and the glass surface. In addition, the geometric inaccuracies, particularly visible in the thin PDMS beams connecting the resonators to the frame, see Figs. 1(a) and 1(d), suggest that geometric stochasticity may play a role in bandgap width. The contributions of all of these effects are quantified in Sec. IV.

The metamaterial with the PDMS frame is further analyzed in Configurations 2 and 3. These TL curves are also depicted in Fig. 2. As expected, two bandgaps may be identified in Configuration 2, induced by the hierarchical design, while, in Configuration 3, it appears that the bandgap in Configuration 1 has merged with the first bandgap of Configuration 2, leading to an ultrabroad first bandgap. Specifically, the GMGR of the first bandgap in Configuration 3 is of 81.8%, which surpasses that of most resonant, elastic metamaterials—GMGRs are often in the range of 13.4–65.5%.[10,11,14,21–23] It should be noted though that the measurements for bandgap width can be quite sensitive to the metric used. GMGR was here chosen for its capability to compare bandgaps of different frequency ranges and depths.
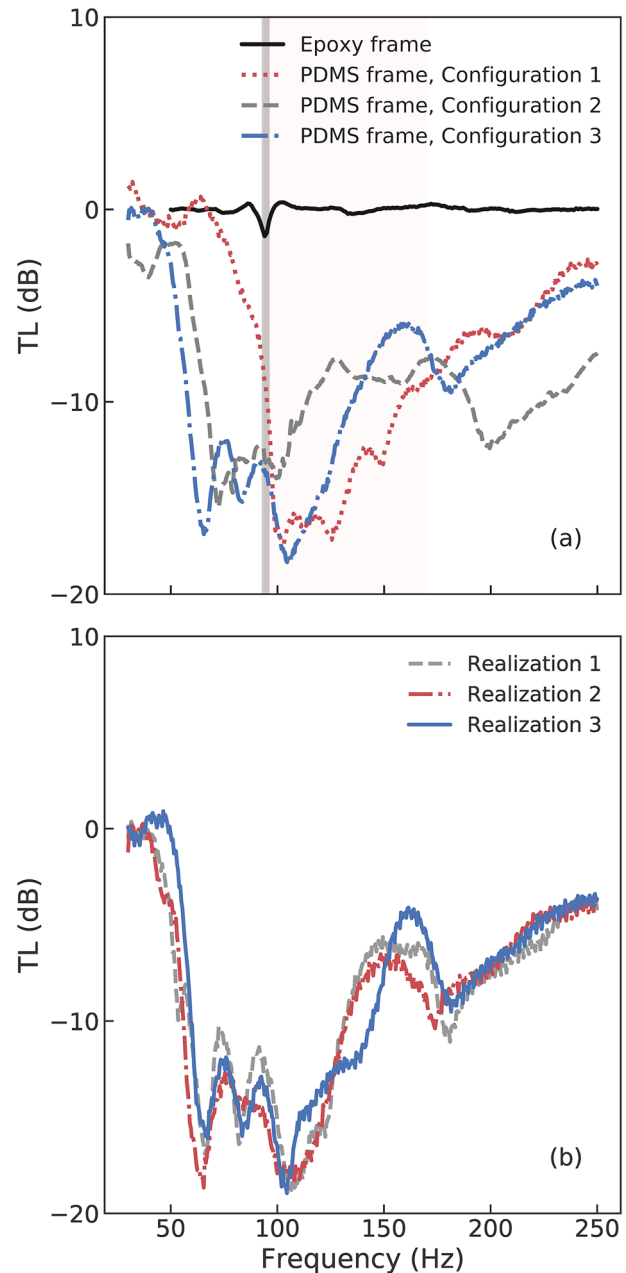
FIG. 2. (a) TL curves for the epoxy frame and each of the tested configurations for the PDMS frame (average over three experimental realizations). Bandgaps for the epoxy frame and the PDMS frame in Configuration 1 are highlighted in gray and red, respectively. (b) Three experimental realizations of the TL curve of Configuration 3 with the PDMS frame.

Finally, we note that the experimental transmission loss curves for the metamaterial with PDMS frame in Configurations 1, 2, and 3 in Fig. 2(a) are averages over three realizations—these are depicted in Fig. 2(b) for the case of Configuration 3. The observed differences

between distinct realizations, which can reach 15 Hz for the location of the minimum TL, are likely induced by the random insertion and reinsertion of insets and subsequent differences in lubrication. Despite this, we observe a similar overall structure, which we aim to capture in numerical simulations.

III. MODELING

To enable a direct comparison with the experimental data, we use COMSOL Multiphysics® (Ref. 24) and the solid mechanics module to model the finite system with the finite element (FE) method. The wave propagation behavior of the additively manufactured elastic metamaterials is investigated in 2D plane stress with linearized kinematics due to the small displacements observed experimentally. The majority of the FE simulations are performed using frequency domain studies with the exception of when friction being included. In the latter case, time-dependent studies are necessary. For the frequency domain studies, the ratio of u_{out} to u_{in} in Eq. (1) is computed directly using the amplitude of the harmonic signal at two points chosen near the input excitation and at the opposite end of the sample. For the time-dependent simulations, we obtain u_{in} and u_{out} in a manner similar to the experiments described in Sec. II, where the integration is here done over the last five cycles.

The details of the computational domain used to model the metamaterial are depicted in Fig. 15 for Configuration 2. Its dimensions are directly obtained from the experimental sample, with the exception of the beams. These are idealized as two sets of identical rectangles for the L1 and L2 units, with thicknesses chosen to match their measured average effective stiffness in the longitudinal direction (3250 N/m and 2840 N/m, respectively). The spatial variability of the beams' thickness and resulting stiffness (experimentally quantified to be ± 623 N/m for units L1 and ± 157 N/m for units L2) is also later studied in order to quantify the accuracy of such an idealization on the transmission loss curves. The meshes for Configurations 1, 2, and 3 contain 24,162, 36,082, and 31,312 triangular elements, respectively, and quadratic shape functions are used for the finite element analysis. In all three cases, a generalized-α method with $\alpha = 0.95$ is used for the time integration.[25]

TABLE I. Density ρ and elastic material properties (Young's modulus E and Poisson's ratio ν) for PDMS and steel.

Material	E (Pa)	ν	ρ (kg/m³)
PDMS	2.99×10^6	0.49	1100
Steel	210×10^9	0.29	7183

For our initial examination, a purely elastic model is used for all the phases, based on uniaxial test experimental data. We quickly surmise that this purely elastic model will likely not be sufficient for predictive modeling as PDMS is known to have viscoelastic properties. Thus, we also use a generalized Maxwell model,[26] whose parameters have been obtained from fitting a Prony series to frequency-dependent storage and loss modulus data from dynamic mechanical analysis (DMA) testing. Figure 3 shows the frequency-dependent storage and loss modulus data together with two possible models to fit the data. These models are consistent with the DMA data in the experimentally available frequency range but behave qualitatively different upon extrapolation, particularly for the loss modulus. For Model 1, the loss modulus monotonically increases with frequency in the range of interest, as is expected for rubbers,[27] while Model 2 exhibits a maximum followed by a rapid decay. Consideration of these two models will provide an understanding of the impact of the different relaxation rates on the overall metamaterial response, as well as will help assess the impact of model uncertainty on the numerical results. The material parameters involved in the elastic and viscoelastic constitutive relations are detailed in Tables I–III.

Our sample makes contact with a glass surface, lubricated with oil, resulting in external dissipation due to friction. It is known that for lubricated friction, the friction coefficient may vary with speed and can actually decrease by one to two orders of magnitude.[28] Due to the difficulties in modeling the complex tribology, we use a simple Coulomb friction model and examine its effect on the TL curve. We note that for numerical purposes, a regularized version of the Coulomb friction model is used:
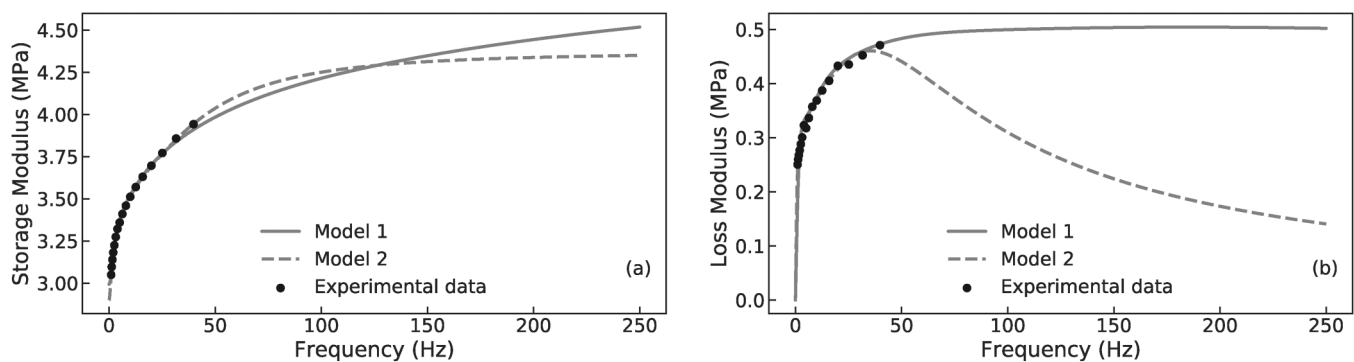
FIG. 3. Experimental data for the (a) storage modulus and (b) loss modulus of PDMS, together with two Prony series models, labeled as Models 1 and 2. Refer to Tables I–III for fit parameters.

TABLE II. Prony series parameters for Model 1.

Tensile modulus (MPa)	Relaxation time (s)
2.9937	∞
0.4488	0.059 56
0.3858	0.009 199
0.4327	0.002 624
0.4750	0.000 703 6
0.8820	0.000 1

TABLE III. Prony series parameters for Model 2.

Tensile modulus (MPa)	Relaxation time (s)
2.8998	∞
0.3628	0.1298
0.3282	0.0222
0.7812	0.0037

$$\mathbf{F} = \frac{-\mu N}{\sqrt{v_x^2 + v_y^2 + \epsilon}}, \begin{pmatrix} v_x \\ v_y \end{pmatrix}, \tag{3}$$

where the force $\mathbf{F}$ is given by the coefficient of friction μ, the magnitude of the normal force N, the velocity components v_x and v_y, and the regularization factor, ϵ. The addition of this factor enables larger time steps and, therefore, shorter computational time, though this must be sufficiently small so that its effect on the TL curve is negligible. The resonators are the only part of the sample to contact the glass surface, and, in the simulations, friction is considered to be applied to the resonators along their mid-surfaces in order to satisfy the conditions of plane stress.

To complement the FE simulations, we consider a 1D mass-spring-damper model as shown in Fig. 4 with 15 masses to represent Configuration 1 without hierarchical designs. This simplified model and several particularizations of it will allow us to distill the essence of various effects (frame stiffness, viscoelasticity, and friction) and qualitatively assess their impact on the observed behavior. In this model, the masses m, representing the frame, are connected to each other via standard linear solid (SLS) elements, which include a spring and a Maxwell arm in parallel. The spring constant k_0 is chosen to represent the frame stiffness and is determined by applying a uniaxial extension in a periodic finite element analysis. Attached to each mass is a resonator with mass m_r, representing the L1 inset, also connected via SLS elements to the frame. k_0^r corresponds to the effective stiffness of the L1 inset and is directly taken from measurements of the sample.

To further guide our understanding of the bandgaps in the TL diagrams, we perform additional unit cell analyses for infinite periodic media. These are also carried out using COMSOL Multiphysics®.

IV. RESULTS AND DISCUSSION

Many effects, integral to achieving agreement between experimental and numerical results, have been considered during the
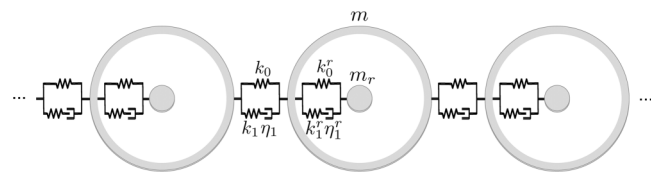
FIG. 4. A mass-spring chain with resonators connected via SLS type models.

modeling process such as frame stiffness, viscoelasticity, friction, and geometric stochasticity in the beams. As we will see, these can affect to differing degrees whether or not bandgaps are detectable in the first place, the widths of bandgaps, and our ability to combine bandgaps from different types of resonators. To understand their individual contribution, we start by examining the purely elastic model as a reference and then measure the impact of these four effects on the TL diagrams.

A. Elasticity

Starting with the purely elastic model, comparisons between numerical simulations and the experimental results for the metamaterial with PDMS frame are shown for each configuration in Fig. 5. TL curves in the numerical simulations differ greatly from the experiments. They are deeper and narrower, possess enhanced transmission peaks due to Fabry–Pérot oscillations,[8] and underestimate the location of the bandgaps—especially, in the cases of the higher frequency bandgaps in Configurations 2 and 3. These differences are strong indicators that viscoelastic effects that can dampen wave propagation and increase the dynamic stiffness of the material need to be considered.

B. Frame stiffness

Before exploring the improvements that viscoelasticity can add beyond the purely elastic model, we seek to explain why during the experiments and in numerical simulations, we can barely detect the bandgaps using a stiffer frame (epoxy) as seen in Fig. 2, while the PDMS frame delivers a surprisingly broad bandgap. To understand this drastic difference in behavior, we present TL diagrams for several intermediate frame stiffnesses in Fig. 6 for Configuration 1. One TL curve corresponds to the Young's modulus of the original PDMS frame (E_{PDMS}). The other five TL curves correspond to frames with Young's modulus 2, 5, 10, 100, and 1000 times E_{PDMS}, the latter being approximately equal to the Young's modulus for epoxy. Figure 6 depicts a monotonic decrease in bandwidth (for the first bandgap) with an increase in frame stiffness, until it is nearly undetectable, similar to what is observed in the experiments, see Fig. 2. This trend can be partially explained by examining the dispersion relation for the 1D mass-spring system described earlier without viscous damping or friction applied to the resonators. As shown in Fig. 7, the imaginary part of the wave number is reduced in the bandgap for the stiffer frames, indicating reduced attenuation[29] and, therefore, shallower TL curves. However, this mechanism does not explain the sharp dip at the right edge of the first bandgap for the PDMS frame, as observed in Fig. 6. The TL curves for frames with Young's modulus 2, 5, and 10 times E_{PDMS} suggest that an additional resonant bandgap exists. Its frequency range decreases with frame
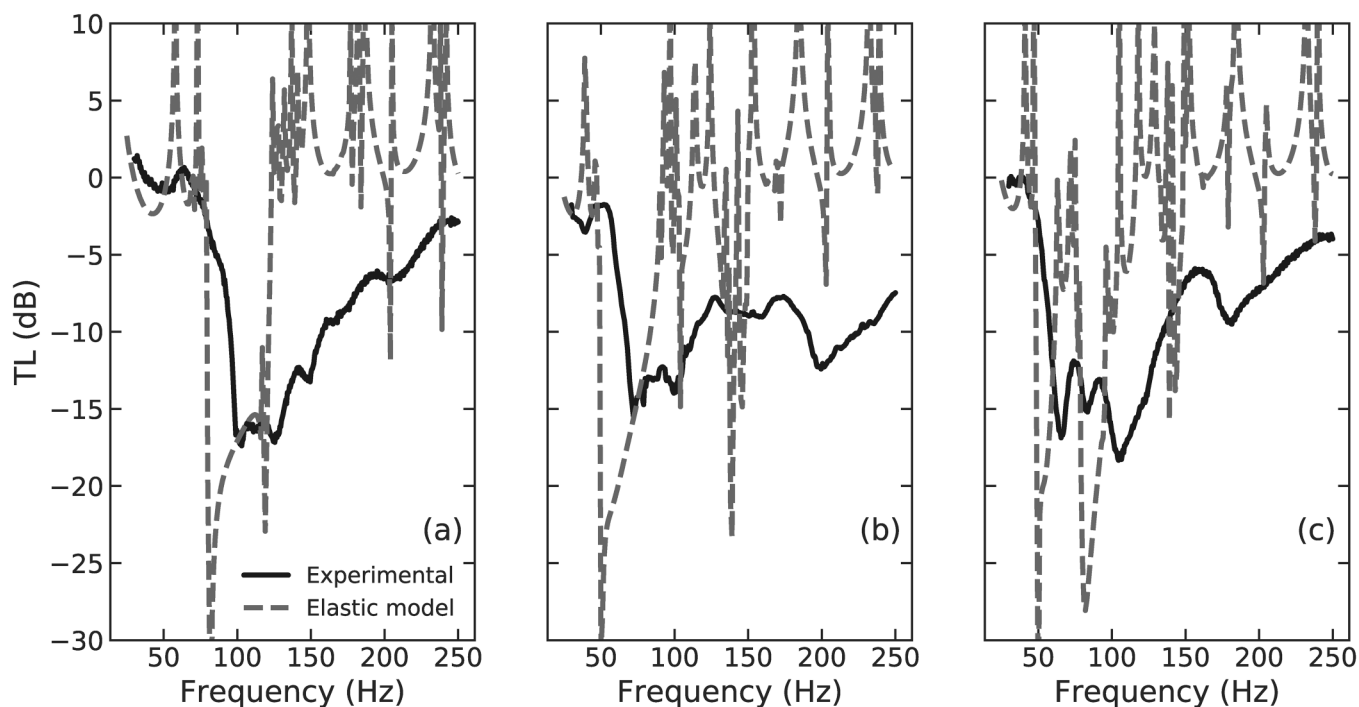
FIG. 5. Comparison between experimental and numerical TL results with elastic constitutive behavior for (a) Configuration 1, (b) Configuration 2, (c) Configuration 3, all using a PDMS frame.
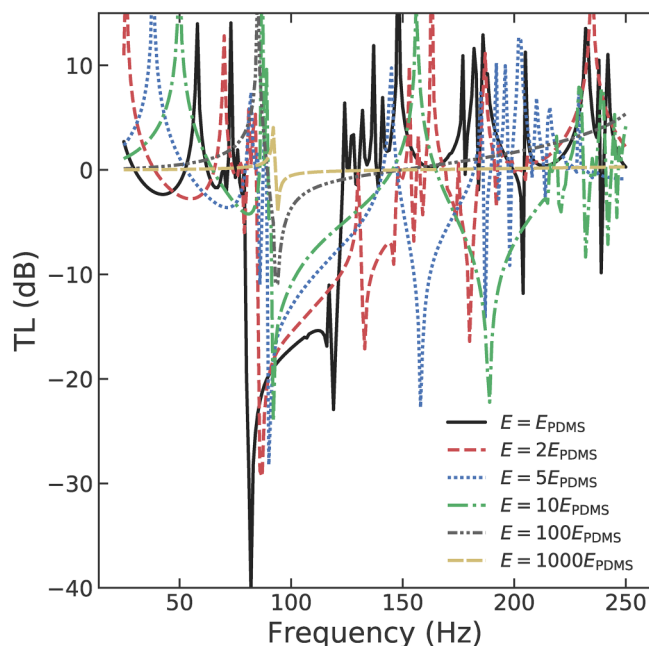
FIG. 6. Numerical results for TL curves for a system in Configuration 1 with various frame stiffnesses and a purely elastic model.
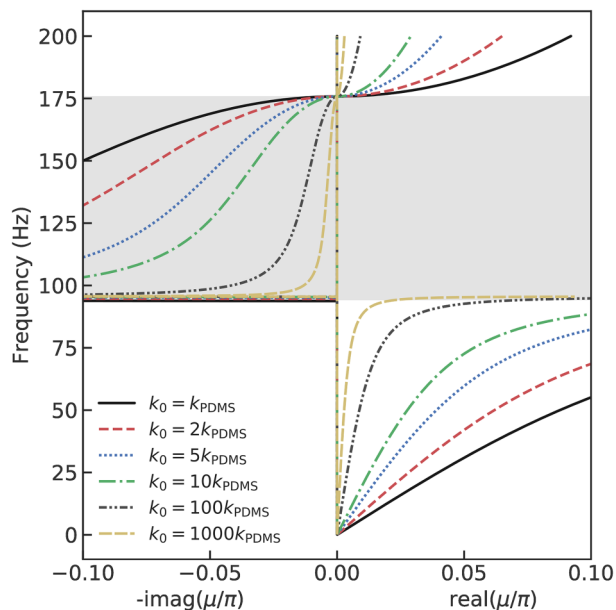
FIG. 7. Dispersion relations for 1D resonant mass-spring systems (elastic analog of Fig. 4) with different frame stiffness k_0. The other parameters are common to all systems: $k_{PDMS} = 21.206$ kN/m, $k_r = 3.250$ kN/m, $m = 3.782$ g, and $m_r = 9.010$ g.

compliance and potentially merges with the first bandgap for the PDMS frame. A detailed analysis of the displacement field in the resonators resulting from the TL calculations (see Fig. 8 for epoxy and PDMS and Sec. I of the supplementary material for intermediate stiffness values) is indicative of this phenomenon. While the first bandgap for frame stiffness beyond E_{PDMS} is associated with resonators mainly oscillating in the horizontal direction, the second one is dominated by vertical and rotational modes. Interestingly, for the PDMS frame, the bandgap exhibits both sets of modes near the left and right edge of the bandgap, respectively. Unit cell analyses for infinite periodic media further confirm this observation. Figures 9(a) and 9(b) show the resulting band diagram along the ΓX direction together with the Bloch modes along the various branches for both the epoxy and PDMS frames respectively (analogous figures

for intermediate frame stiffness are given in Sections II–VI of the supplementary material). In all cases, one pair of branches, shown with solid red lines, contains modes with displacements primarily in the horizontal direction whose resulting bandgap is marginally affected by a change in frame stiffness. In contrast, the other pair of branches, shown with dashed blue lines, primarily contains rotational and vertical modes with edges that significantly shift to higher frequencies as the frame stiffness increases. All of these observations combined suggest that the ultrabroad first bandgap observed for the PDMS frame partially results from the merging of two bandgaps.

Thus, the effect of lowering the compliance of the frame on the bandgap structure is twofold. Not only do we see the widening of the existing bandgap induced by the resonators, we see completely new vibrational modes in the frequencies explored that
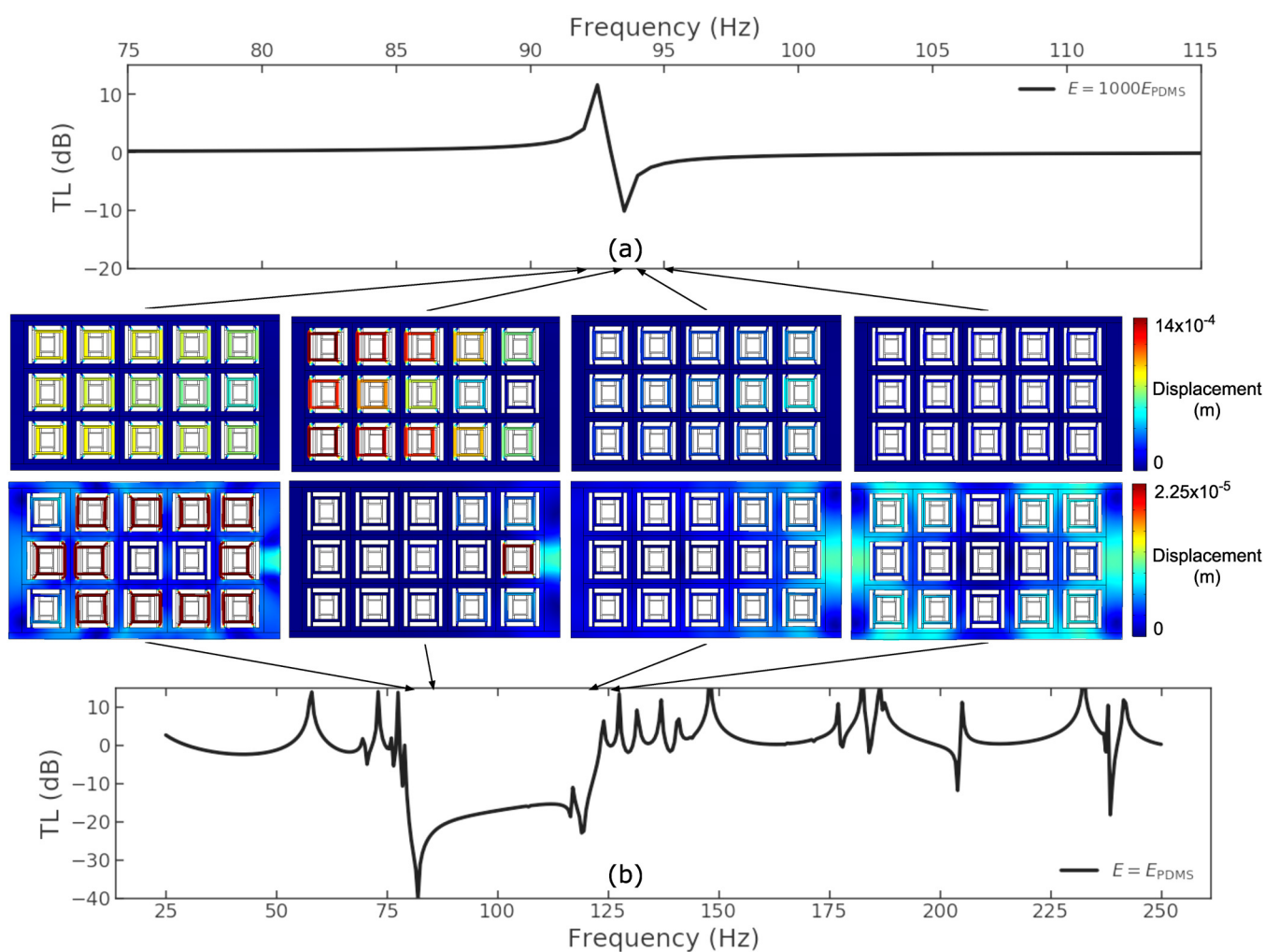
FIG. 8. (a) TL diagram for frame stiffness $E = 1000E_{PDMS}$ along with displacement fields for 92, 93, 94, and 95 Hz, respectively. (b) TL diagram for frame stiffness $E = E_{PDMS}$ along with displacement fields for 78, 82, 122, and 125 Hz, respectively. For the above simulations the total displacement is depicted. Free boundary conditions are applied everywhere except for a portion of the right edge of the sample where a harmonic displacement is applied.
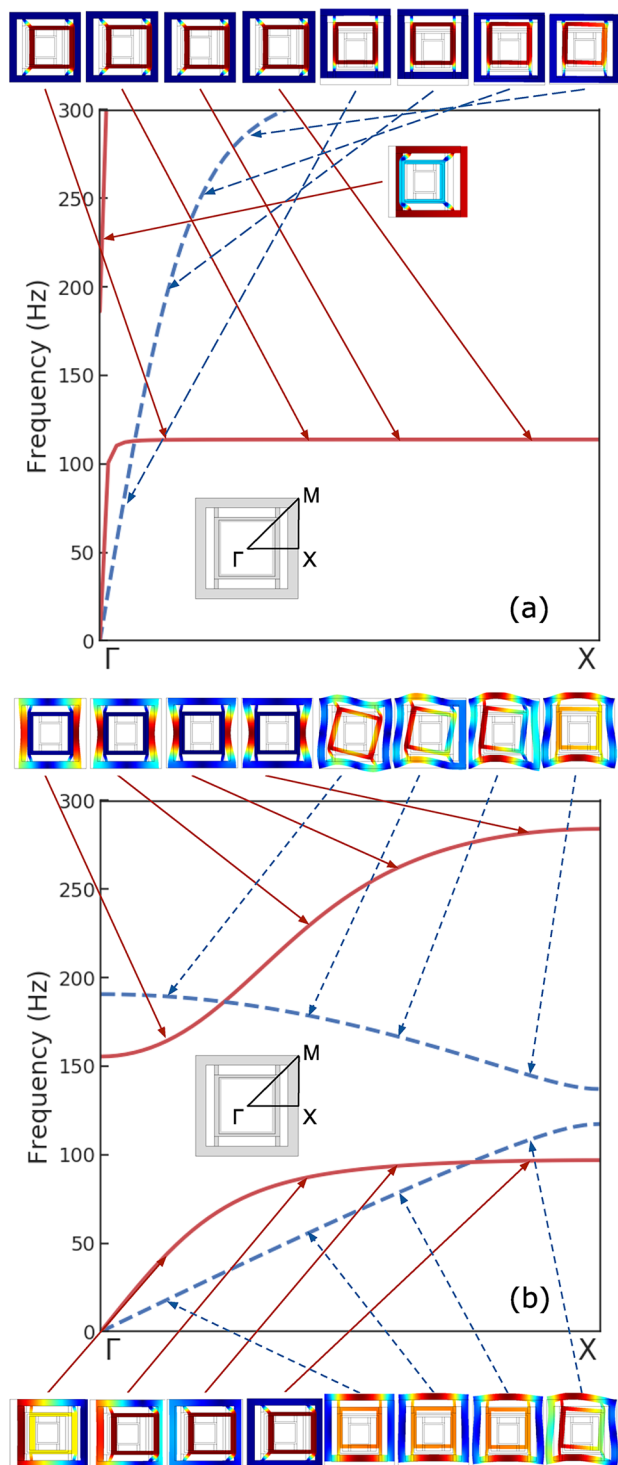
FIG. 9. Band diagram for a unit cell of the elastic metamaterial with (a) epoxy and (b) PDMS frames along the ΓX direction. Bloch modes shown with arrows pointing to their corresponding locations on each branch.

did not manifest in the stiffer frame. These new modes are associated with a second bandgap whose frequency range is strongly dependent on the frame stiffness. For the PDMS frame, this second bandgap merges with the first one to form a single ultrabroad bandgap. These results, therefore, highlight the importance of frame compliance for optimizing attenuation performance in resonant metamaterials.

A related bandgap widening effect, termed the "trampoline effect," has been reported in other studies.[30–33] In these works, the authors examine stubbed plate systems and find similar increases in bandwidth by adding holes to the plate effectively reducing its stiffness. The addition of the holes does, however, also alter the mass of the plate and introduces new free boundaries that could further affect the wave propagation behavior. This is in contrast to the work presented here where the effect of the stiffness has been completely isolated, and the resonant units are not axisymmetric. The later could provide added flexibility for independently tuning various bandgaps. It is important to remark though that there is not a universal dependence between bandwidth and depth and matrix stiffness across different resonant, elastic metamaterial systems. As a counterexample of the above observed trend, the authors in Ref. 14 also studied a stubbed plate system without holes and find that increasing the stiffness of the plate increases the width and frequency of the bandgaps in their system. Further non-monotonic behavior of the bandwidth has been observed with changes in geometric features of a given metamaterial.[34,35] All of these influences combined highlight the complexities of designing and optimizing metamaterials with desired dynamical properties.

C. Viscoelasticity

Now that the effects of frame stiffness have been examined in detail, we address the impact of material viscoelasticity on the dynamic response. As mentioned before, the tell-tail signs seen in the TL curves from the purely elastic model in Fig. 5 (deeper and narrower bandgaps, enhanced transmission peaks, and low estimates for bandgap frequencies) indicate that viscoelastic effects play a large role in the experimental results. Using Models 1 and 2 as described in Sec. III for the constitutive relation of the PDMS phase, Fig. 10 shows the TL results after adding viscoelasticity to the numerical model in Configurations 1, 2, and 3. Compared to the completely elastic model, the addition of viscoelasticity causes bandgaps to shift to higher frequency, reduce their depth, and increase their widths, in greater agreement with the experimental results. The observed effects of viscoelasticity are consistent with previous studies[9] and can be intuitively understood from the mass-spring model in Fig. 4. Indeed, for the limiting cases of zero and infinite damping coefficient, the effective stiffness of the SLS element of the resonator ranges between k_0^r and $k_0^r + k_1^r$, respectively, and is thus always increased by the addition of Maxwell arms. The results of Fig. 10 also depict locations and widths of the first bandgap in all configurations that are very close to each other for Models 1 and 2. This, therefore, indicates that the experimentally available DMA data are sufficient for such purposes. We recall that both Model 1 and 2 match the experimental storage and loss modulus data in the lower frequency range and primarily differ in
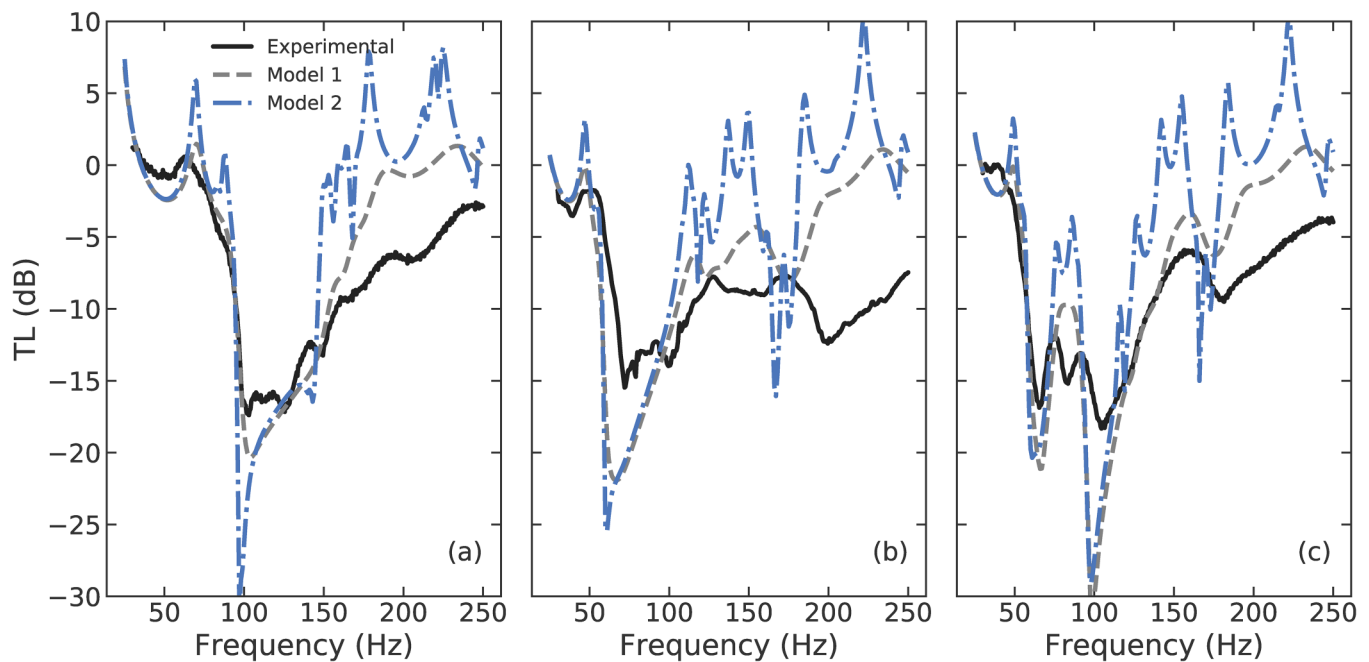
FIG. 10. Comparison of experimental results to finite element results with viscoelastic constitutive behavior (for both Model 1 and Model 2) for (a) Configuration 1, (b) Configuration 2, and (c) Configuration 3, all using a PDMS frame.

the extrapolation of the loss modulus at higher frequencies, see Fig. 3. This difference results in different levels of suppression of the enhanced transmission peaks, particularly, at high frequencies and results in the more realistic model (Model 1) to be in better agreement with the experimental results.

A detailed comparison between the TL curves in Fig. 5 with the purely elastic model and those of Fig. 10 with viscoelastic constitutive relation further shows that the bandgap widening effect of viscoelasticity is useful for combining bandgaps in multiresonant structures. More specifically, Configuration 3, where L2 insets are added to every odd column (i.e., it is a combination of Configurations 1 and 2), clearly depicts three bandgaps in Fig. 5(c), at frequencies that are consistent with the bandgap of the single resonator in Configuration 1 and the two bandgaps of the hierarchical design in Configuration 2. With the addition of viscoelasticity, the first two bandgaps of Configuration 3 merge, as shown Fig. 10(c). This results in an ultrabroad low-frequency bandgap, in strong agreement with the experimental TL data.

D. Friction

Next, we seek to understand the role of external dissipation (friction) on the TL curves, for which time-dependent simulations are performed with Coulomb friction applied to the resonators. The results are shown in Fig. 11, where it is observed that friction further reduces the depth of some of the bandgaps, though this behavior does not appear to be monotonic throughout the whole frequency range examined. Yet, contrary to what occurs with

viscoelasticity, frictional effects do not seem to increase or shift the range of bandgap frequencies (to this we remark that care needs to be taken when choosing the time step in the numerical simulations with friction and that a too large time step may artificially induce a shift in the bandgap frequency). A fully analogous effect is observed when including friction in the one dimensional mass-spring-model of Fig. 4. In Fig. 12, the elastic case with no dissipation is shown for reference along with the results for three friction coefficients. As seen, the attenuation effect within the bandgap is greatly reduced with friction and this effect monotonically increases with the friction coefficient. Again, no shift of the bandgap frequency is observed with the addition of friction.

E. Geometric stochasticity

Finally, we consider the effects of geometric imperfections of the PDMS beams on the TL curves. Experimentally, such imperfections have been quantified through the stiffness of a unit cell with the L1 inset, which is 3250 ± 623 N/m in the longitudinal direction. This 623 N/m uncertainty approximately corresponds to a 10% change in beam width (assuming the 4 beams of a resonant unit are identical) and to a 9.4 Hz uncertainty in the resonant frequency for the L1 units. The former is consistent with the measured standard deviation in beam width, approximately of 7%.

To better understand the effects of beam stochasticity on the TL diagram for Configuration 1, we examine two cases, both using the viscoelastic Model 1. The first, shown in Fig. 13, considers that each of the four beams have random beam widths drawn from a
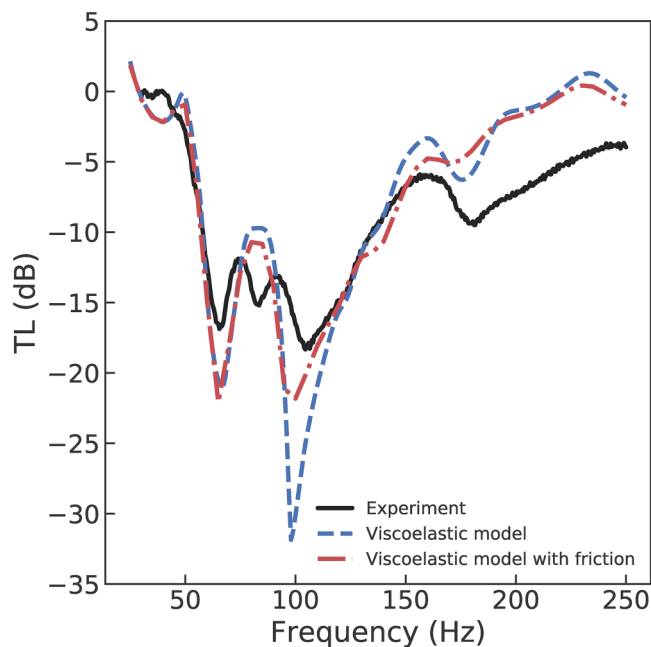
FIG. 11. Experimental results compared to numerical results including viscoelasticity and friction in addition to viscoelasticity for Configuration 3 (all using a PDMS frame).
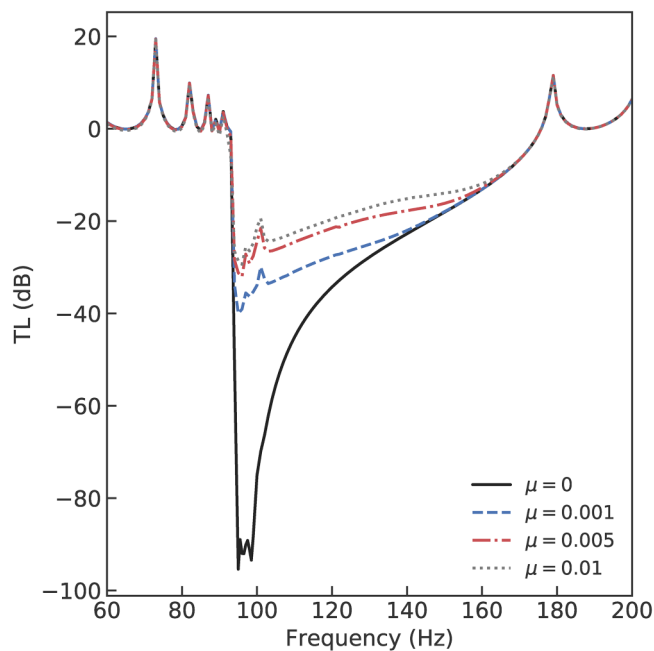
FIG. 12. TL curves for the 1D mass-spring-resonator system (elastic analog of Fig. 4) with various values of the friction coefficient μ (including the frictionless case of $\mu = 0$).

Gaussian distribution, with 10% and 20% of the beam width as the standard deviation for subfigures (a) and (b), respectively. In either case, the variability on the TL curve is not found to be significant as compared to the deterministic case, and only a mild increase in
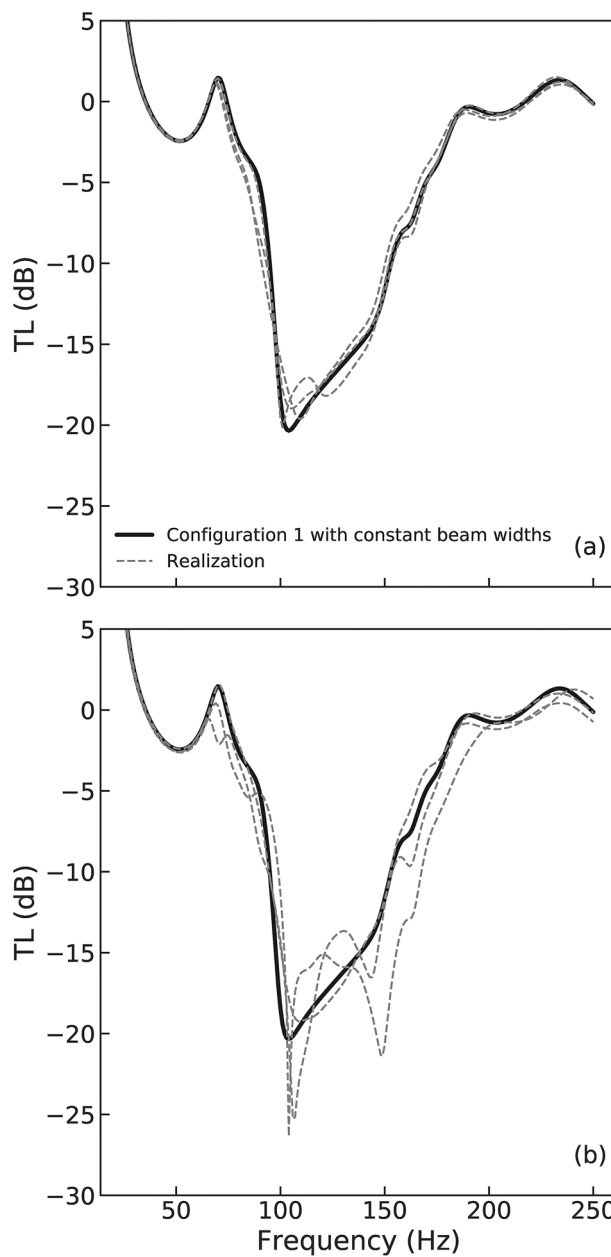
FIG. 13. Effects of stochasticity in the beam widths for (a) 10% of beam width standard deviation and (b) 20% of beam width standard deviation. The black, solid lines represent the TL for Configuration 1 with constant beam widths, and the gray, dashed lines represent various realizations of the TL for stochastic beam widths. In all cases, the viscoelastic Model 1 has been used in the simulations.

bandwidth is observed for the 20% case. The second scenario examined is aimed at accounting for imperfect alignment of the manual insertions of the insets in the PDMS pockets. More specifically, an insertion at a rotated angle could potentially change the frequency spectrum of the vibrational modes of the system and induce a change in the TL diagram. To mimic this effect, we here consider that one pair of diagonal beams has random beam widths and another pair has constant beam widths. The results for this case are qualitatively similar to the former one, and its figure is thus omitted for brevity in the exposition.

With all effects considered, it may thus be concluded that the measured stochasticity in the beam widths has a small effect on the TL curves and thus measuring the mean effective stiffness of the units represents sufficient elastic information to predict the location of the bandgaps.

V. CONCLUSION

Using additively manufactured elastic metamaterials, we study the role of frame stiffness, viscoelasticity, friction, and stochasticity in wave attenuation performance. The first of these effects, frame stiffness, plays a surprisingly important role in the broadening of bandgaps with a dual effect on the structure of the TL curve. Increasing the compliance of the frame (matrix) material first increases the magnitude of the imaginary part of the dispersion relation, which results in a wider bandgap while maintaining the overall structure. The added compliance can also aid in tuning the different resonant bandgaps (i.e., horizontal and vertical) and potentially merging them. Also, aiding in the broadening and shifting of bandgaps (in this case to higher frequencies) is viscoelasticity. Interestingly, all of these effects combined (frame compliance and viscoelasticity) proved to be powerful mechanisms to merge bandgaps from different types of resonators and form ultrabroad low-frequency bandgaps. Specifically, the metamaterial with PDMS frame in Configuration 3 achieves, without having performed any optimization in its design, a GMGR of 81.8%, surpassing that of many examples seen in the previous literature.

Although the other two phenomena (friction and stochasticity) did not play a critical role in shaping the TL curve for the specific metamaterial studied, interesting practical considerations resulted from the analyses. In particular, friction mainly served to reduce the amount of attenuation in the bandgap while maintaining the edges of the bandgap intact. Yet, it was found that incorrect choices in time steps can result in numerical errors that can shift the entire TL curve to lower frequency ranges. As for stochasticity in the beam widths, it was found that variations of the order of 10% common in thin structures that are fabricated with additive manufacturing (or even larger—until 20%) did not lead to significant variations on the bandgap frequency or width. Measuring the effective stiffness of each unit was, therefore, enough to obtain good predictions in the TL diagram. Finally, we note that although limited amount of DMA data was experimentally available to characterize the viscoelastic behavior of PDMS (specifically from 0–50 Hz), such data ended up being the most important for predicting the location and width of the bandgaps below 200 Hz, as assessed with two viscoelastic models that were markedly distinct beyond 50 Hz.

SUPPLEMENTARY MATERIAL

See the supplementary material for a video showing the 3D printing process using DIW for the beams along with additional unit cell analyses and more detailed plots showing the motions of the resonators in Configuration 1.

APPENDIX A: FABRICATION AND EXPERIMENTS

To prepare the 3D printable PDMS ink, we first mixed SE 1700 and Sylgard 184 (both Dow Corning) in a weight ratio of 85:15, each with a 10:1 cross-linker ratio. The material was then mixed in a vacuum mixer (SpeedMixer DAC 600 VAC by FlackTek) at 1650 rpm for 1 min and 45 s under 20 Torr vacuum. The mixed material was then transferred into a syringe and centrifuged at 3400 rpm for 13 min. The beams and outlines of the structures were
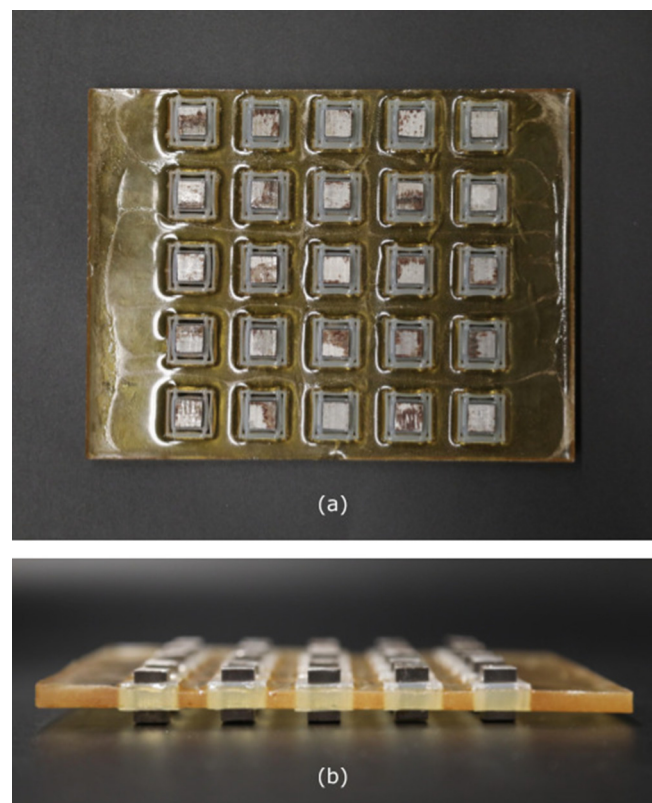
FIG. 14. (a) Elastic metamaterial with epoxy frame. (b) Side profile of the elastic metamaterial with epoxy frame.
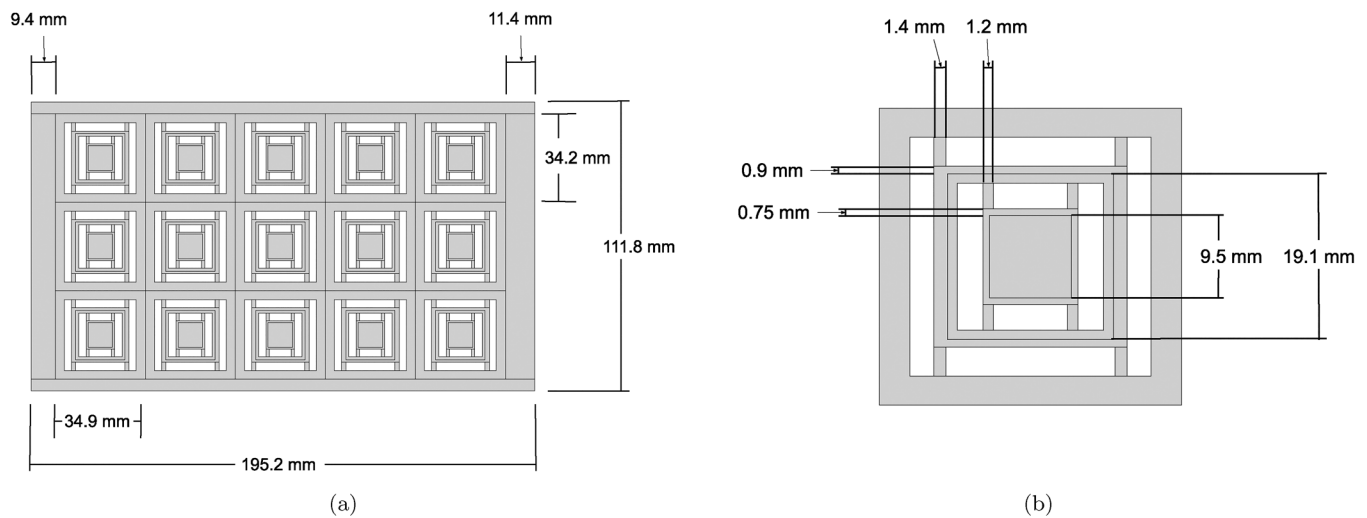
FIG. 15. (a) Schematic of the computational domain of the complete sample in Configuration 2 and (b) one of its unit cells.

subsequently printed using DIW, an extrusion-based 3D printing method (video included in supplementary material). The PDMS ink was extruded from a $400\,\mu m$ nozzle under constant pressure. These were then thermally cross-linked at $100\,°C$ for 1 h. The outer frame was then casted using either PDMS or epoxy. If PDMS was used, a subsequent curing step at $100\,°C$ was used. If instead epoxy was used, a low-viscosity epoxy resin (mixture of Hexion Epon^{TM} 828 and its cross-linker Epikure^{TM} 3223 in weight ratio of 3:1) was injected into the PDMS outline and subsequently cross-linked at $60\,°C$ for 2 h. The steel parts, with masses of 8.5 g and 9.8 g for the L1 and L2 insets, respectively, were then inserted manually at the desired locations. The completed sample is shown in Fig. 1 for the PDMS frame and Fig. 14 for the epoxy frame.

Two PCB Piezotronics, Inc., accelerometers were glued to the two ends of the elastic metamaterial to collect input and output signals, respectively. A mechanical shaker (APS Dynamics 113) was attached with the sample and programmed to input a sinusoidal mechanical wave. A frequency sweep from 30 to 250 Hz was set at the input end. Digital acquisition was performed by a National Instruments cDAQ-9171 at a rate of 12 800 pts/s.

APPENDIX B: NUMERICAL SIMULATIONS

In this section, we include a schematic of the computational domain, which is shown in Fig. 15.

DATA AVAILABILITY

The data that support the findings of this study are available within the article.

REFERENCES

[1]G. Milton and J. Willis, "On modifications of Newton's second law and linear continuum elastodynamics," Proc. R. Soc. A **463**, 855–880 (2007).

[2]Y. Liu, X. Su, and C. T. Sun, "Broadband elastic metamaterial with single negativity by mimicking lattice systems," J. Mech. Phys. Solids **74**, 158–174 (2015).

[3]Z. Liu, X. Zhang, Y. Mao, Y. Y. Zhu, Z. Yang, C. T. Chan, and P. Sheng, "Locally resonant sonic materials," Science **289**(5485), 1734–1736 (2000).

[4]M. Addouche, M. A. Al-Lethawe, A. Elayouch, and A. Khelif, "Subwavelength waveguiding of surface phonons in pillars-based phononic crystal," AIP Adv. **4**(12), 124303 (2014).

[5]A. Sukhovich, B. Merheb, K. Muralidharan, J. O. Vasseur, Y. Pennec, P. A. Deymier, and J. H. Page, "Experimental and theoretical evidence for subwavelength imaging in phononic crystals," Phys. Rev. Lett. **102**, 154301 (2009).

[6]A. N. Norris and A. L. Shuvalov, "Elastic cloaking theory," Wave Motion **48**(6), 525–538 (2011).

[7]M. I. Hussein, M. J. Leamy, and M. Ruzzene, "Dynamics of phononic materials and structures: Historical origins, recent progress, and future outlook," Appl. Mech. Rev. **66**, 040802 (2014).

[8]Y. F. Wang, Y. S. Wang, and V. Laude, "Wave propagation in two-dimensional viscoelastic metamaterials," Phys. Rev. B **92**, 104110 (2015).

[9]M. A. Lewińska, V. G. Kouznetsova, J. A. W. van Dommelen, A. O. Krushynska, and M. G. D. Geers, "The attenuation performance of locally resonant acoustic metamaterials based on generalised viscoelastic modelling," Int. J. Solids Struct. **126–127**, 163–174 (2017).

[10]M. V. Barnhart, X. Xu, Y. Chen, S. Zhang, J. Song, and G. Huang, "Experimental demonstration of a dissipative multi-resonator metamaterial for broadband elastic wave attenuation," J. Sound Vib. **438**, 1–12 (2019).

[11]S. Krödel, N. Thomé, and C. Daraio, "Wide band-gap seismic metastructures," Extreme Mech. Lett. **4**, 111–117 (2015).

[12]H. Meng, D. Chronopoulos, A. T. Fabro, W. Elmadih, and I. Maskery, "Rainbow metamaterials for broadband multi-frequency vibration attenuation: Numerical analysis and experimental validation," J. Sound Vib. **465**, 115005 (2020).

[13]A. Colombi, D. Colquitt, P. Roux, S. Guenneau, and R. V. Craster, "A seismic metamaterial: The resonant metawedge," Sci. Rep. **6**, 27717 (2016).

[14]P. Celli, B. Yousefzadeh, C. Daraio, and S. Gonella, "Bandgap widening by disorder in rainbow metamaterials," Appl. Phys. Lett. **114**(9), 091903 (2019).

[15]K. T. Tan, H. H. Huang, and C. T. Sun, "Optimizing the band gap of effective mass negativity in acoustic metamaterials," Appl. Phys. Lett. **101**(24), 241902 (2012).

[16]C. Liu and C. Reina, "Broadband locally resonant metamaterials with graded hierarchical architecture," J. Appl. Phys. **123**(9), 095108 (2018).

[17]P. Wang, F. Casadei, S. Shan, J. C. Weaver, and K. Bertoldi, "Harnessing buckling to design tunable locally resonant acoustic metamaterials," Phys. Rev. Lett. **113**, 014301 (2014).

[18]D. M. Kochmann and K. Bertoldi, "Exploiting microstructural instabilities in solids and structures: From metamaterials to structural transitions," Appl. Mech. Rev. **69**(5), 050801 (2017).

[19]R. Zhu, Y. Y. Chen, M. V. Barnhart, G. K. Hu, C. T. Sun, and G. Huang, "Experimental study of an adaptive elastic metamaterial controlled by electric circuits," Appl. Phys. Lett. **108**(1), 011905 (2016).

[20]L. D'Alessandro, E. Belloni, R. Ardito, A. Corigliano, and F. Braghin, "Modeling and experimental verification of an ultra-wide bandgap in 3d phononic crystal," Appl. Phys. Lett. **109**(22), 221907 (2016).

[21]Y. Tian, J. H. Wu, H. Li, C. Gu, Z. Yang, Z. Zhao, and K. Lu, "Elastic wave propagation in the elastic metamaterials containing parallel multi-resonators," J. Phys. D: Appl. Phys. **52**(39), 395301 (2019).

[22]L. D'Alessandro, E. Belloni, G. D'Alo, L. Daniel, R. Ardito, A. Corigliano, and F. Braghin, "Modelling and experimental verification of a single phase three-dimensional lightweight locally resonant elastic metamaterial with complete low frequency bandgap," in *2017 11th International Congress on Engineered Materials Platforms for Novel Wave Phenomena (Metamaterials)* (IEEE, 2017), pp. 70–72.

[23]Q. Zhang, K. Zhang, and G. Hu, "Tunable fluid-solid metamaterials for manipulation of elastic wave propagation in broad frequency range," Appl. Phys. Lett. **112**(22), 221906 (2018).

[24]See www.comsol.com for COMSOL Multiphysics® v5.4, COMSOL AB, Stockholm, Sweden.

[25]J. Chung and G. M. Hulbert, "A time integration algorithm for structural dynamics with improved numerical dissipation: The generalized-method," J. Appl. Mech. **60**(2), 371–375 (1993).

[26]R. Christensen, *Theory of Viscoelasticity: An Introduction* (Elsevier, 2012).

[27]V. M. Kulik, A. V. Boiko, S. P. Bardakhanov, H. Park, H. H. Chun, and I. Lee, "Viscoelastic properties of silicone rubber with admixture of SiO_2 nanoparticles," Mater. Sci. Eng. A **528**(18), 5729–5732 (2011).

[28]M. Mate and R. W. Carpick, *Tribology on the Small Scale: A Modern Textbook on Friction, Lubrication, and Wear* (Oxford University Press, 2019).

[29]V. Laude, *Phononic Srystals: Artificial Crystals for Sonic, Acoustic, and Elastic Waves*, De Gruyter Studies in Mathematical Physics Vol. 26 (De Gruyter, Berlin, 2015).

[30]O. R. Bilal and M. I. Hussein, "Trampoline metamaterial: Local resonance enhancement by springboards," Appl. Phys. Lett. **103**(11), 111901 (2013).

[31]O. R. Bilal, A. Foehr, and C. Daraio, "Observation of trampoline phenomena in 3D-printed metamaterial plates," Extreme Mech. Lett. **15**, 103–107 (2017).

[32]Muhammad and C. W. Lim, "Dissipative multiresonant pillared and trampoline metamaterials with amplified local resonance bandgaps and broadband vibration attenuation," J. Vib. Acoust. **142**(6), 061012 (2020).

[33]W. Wang, B. Bonello, B. Djafari-Rouhani, Y. Pennec, and J. Zhao, "Elastic stubbed metamaterial plate with torsional resonances," Ultrasonics **106**, 106142 (2020).

[34]K. H. Matlack, A. Bauhofer, S. Krödel, A. Palermo, and C. Daraio, "Composite 3D-printed metastructures for low-frequency and broadband vibration absorption," Proc. Nat. Acad. Sci. U.S.A. **113**(30), 8386–8390 (2016).

[35]S. Li, Y. Dou, T. Chen, Z. Wan, J. Huang, B. Li, and F. Zhang, "Evidence for complete low-frequency vibration band gaps in a thick elastic steel metamaterial plate," Mod. Phys. Lett. B **33**(04), 1950038 (2019).